

A High Power, Large Aperture Doppler He Lidar for Upper Atmospheric Sensing

Peter D. Dragic and Gary R. Swenson

University of Illinois at Urbana-Champaign, Department of Electrical and Computer Engineering, Urbana, IL 61801

James H. Clemmons

University of New Hampshire, Department of Physics, Durham, NH 03824

ABSTRACT

The combination of modern, high-power lasers and large aperture telescopes will lead to a renaissance in ground based high-altitude lidar capabilities. Such systems will give an unprecedented view into regions of the atmosphere where only passive instruments have been used. This allows for dynamic, range-resolved measurements, potentially from a global network of sensors. While an upper-atmospheric metastable helium lidar is but a singular example, the methods may be applied to other constituents and measurement approaches.

1. INTRODUCTION

With sufficient laser power, a Doppler wind and temperature resonance fluorescence lidar would enable rapid and range-resolved measurements of neutral winds and temperatures in the thermosphere and lower exosphere, namely from 300-1000 km in altitude. Fully analogous to well-known metal resonance lidars, such as those based on sodium or iron which probe the mesosphere and lower thermosphere, the proposed upper atmospheric lidar utilizes metastable helium. Metastable He (He*) is generated predominantly by direct impact between ground-state He atoms and energetic photoelectrons, which are created both locally as well as in the geomagnetically conjugate thermosphere during periods of solar illumination. From the metastable level (in the extreme ultraviolet range), there exists a resonance near 1083 nm, also excited by photoelectrons, which has been observed with ground-based spectrometers and interferometers in night airglow [1,2]; where photoelectrons have pumped the neutral He from the 2^3S state to the 2^3P levels from which the subsequent fluorescence at 1083 nm occurs. Laser light in resonance with this infrared transition is absorbed, subsequently radiated in 4π steradians, and collected by a ground- or space-based telescope [3]. Such a system can prove to be a primary player in ground-based investigations of upper thermospheric and exospheric temperature and dynamics, as well as smaller scale wave perturbations that reach these altitudes from below. This will give unprecedented insight into atmospheric dynamics and space weather at these altitudes. Regarding the former, such a lidar will shed light on wave phenomena and coupling from lower regions of the atmosphere, particularly from the mesosphere and lower thermosphere. Regarding the latter, mapping space weather in these regions is important for the space vehicles that occupy them.

Making viable such a system are recent advances in power-scaled solid-state lasers. For example, fiber lasers (at or around 1083 nm) producing in excess of 10 kW (continuous wave) and multi millijoule energies (pulsed) in diffraction-limited beams have now been demonstrated. Coupled with large aperture, ground-based telescopes (such as the Starfire Optical Range in New Mexico, USA or the Southern Astrophysical Research Telescope in Chile), range-resolved (< 10 km) and rapid (< 1 minute) integration times with very high signal-to-noise ratios are possible. On top of the well-known tactical or industrial manufacturing applications, this introduces these light sources to lidar, thereby opening the doorway to enhanced capabilities in long-distance remote sensing. Here, these lidar systems are discussed with the greatest emphasis given to the requisite enabling technologies.

2. METASTABLE HELIUM (He*)

Helium is a light atom and therefore occupies a broader range of altitudes (from the ground to the exosphere) than other atmospheric constituents, such as metals or molecules. In the upper thermosphere and exosphere (300 – 1000 km), solar illumination leads to photoelectrons that may collide with He in the ground state. The resulting energy transfer excites the He, leading to the emission of an infrared (IR) photon whose wavelength (λ) is near 1083 nm and rendering He*. An energy level diagram for the process is shown in Fig. 1(a). The collisions of photoelectrons with

He in the ground state (1^1S_0) leads to the population of the 2^3P energy levels, which quickly decay through the emission of IR photons. The helium atom is then left in the 2^3S_1 state, which has a tremendously long lifetime. Absorption from this excited state is allowed, and therefore there are three absorption lines corresponding to the three $2^3S_1 \rightarrow 2^3P_{0,1,2}$ transitions. At the altitudes of interest, the temperature is around 1000 K and therefore the absorption lineshapes are Doppler broadened, resulting in spectra that have full widths at half maximum (FWHM) of around 5 GHz. In fact, at 1000 K, the $2^3S_1 \rightarrow 2^3P_{1,2}$ transitions are overlapping. The aggregate excited state absorption cross-section spectrum for these two transitions is shown in Fig. 1(b) at both 1000 K and “low temperature” (i.e., Doppler free). The latter is only meant to visually indicate the relative positions of the absorption peaks. Note that the $2^3S_1 \rightarrow 2^3P_0$ transition is somewhat weaker and it is favorable to operate the proposed lidar near the peak absorption cross-section [4]. Since the lifetime of the metastable level is so long, the same He* may be accessed many times before it relaxes back to the ground state.

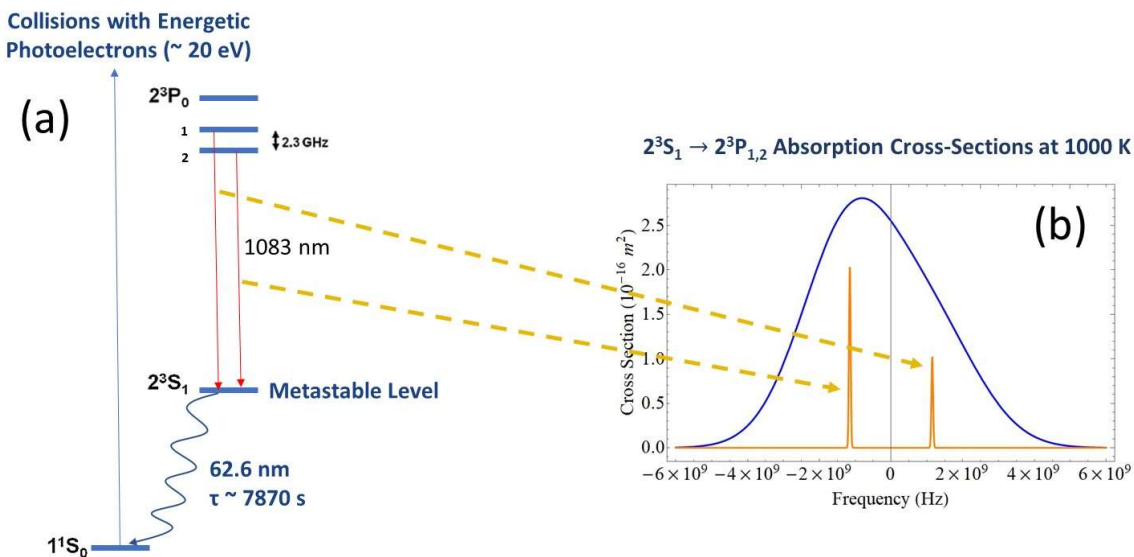


Fig. 1. (a) Energy level diagram for the formation of He*. Ground-state helium is excited into the 2^3P levels through collisions with energetic photoelectrons. Relaxation from 2^3P gives rise to emission near 1083 nm leaving He in the metastable state (He*) 2^3S_1 . The lifetime (τ) of this level is very long, enabling it to be probed with a laser tuned to the absorption. (b) Doppler broadened absorption cross-sections for the $2^3S_1 \rightarrow 2^3P_{1,2}$ transitions. Note that the frequency is relative to the center frequency. The blue curve is the Doppler broadened spectrum at 1000 K while the orange curve is at “low temperature,” i.e., Doppler free. The absorption cross-sections for the $2^3S_1 \rightarrow 2^3P_0$ transition are somewhat lower and are found at a higher frequency.

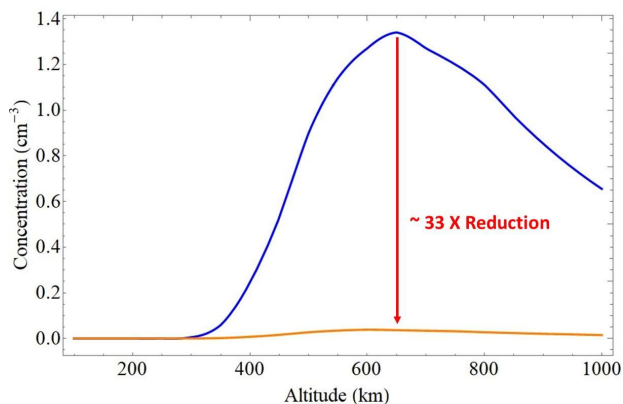


Fig. 2. He* concentration at twilight, 100° SZA, above Arecibo observatory at Winter (blue curve) and Summer (orange curve) Solstices (after [2]). The winter He* concentration is about 33 times higher than in summer.

He* concentrations in the upper atmosphere are relatively low ($\sim 1 \text{ cm}^{-3}$ at its largest) and strongly depend on the season. Due to the larger number of photoelectrons available for exciting He from the ground state [2], the populations in the winter months are much higher than in summer. Fig. 2 shows the He* number density above Arecibo Observatory (Puerto Rico, USA) at both the Summer and Winter Solstices (from [2]). The peak summer concentration is roughly 33 times lower than during the winter months. This plays a significant role in setting the signal-to-noise ratio (SNR) for a lidar system. More details will be provided in a subsequent section.

3. LIDAR EQUATION AND THE THREE FREQUENCY DOPPLER APPROACH

$$N(z) = \underbrace{(\eta T_A^2)}_{\text{System Efficiency}} \underbrace{\left(\frac{P_L \tau_P \lambda}{hc}\right)}_{\text{Number of Transmitted Photons}} \underbrace{(\sigma_{eff} n_s(z) \Delta z)}_{\text{Probability of Scattering}} \underbrace{\left(\frac{A_R}{4\pi z^2}\right)}_{\text{Probability of Receiving}} + \underbrace{N_B \tau_{int}}_{\text{Noise}}$$

Fig. 3. The lidar equation with its components identified.

Fig. 3 displays the basic lidar equation with each of its components identified. The number of detected photoelectrons from altitude (or range) z ($N(z)$) is a strong function of several parameters. The first, system efficiency, possesses two terms. One relates to general system losses (coupling losses, reflections, etc.) and is denoted by the symbol η . T_A is the one-way atmospheric transmittance, which may include scattering losses (Mie and Rayleigh) and absorption by species other than He*. Ideally, system efficiency is close to unity. The second term is the number of transmitted photons, or the pulse energy divided by the energy of a single photon. The pulse energy is the laser power (P_L) multiplied by the pulse duration, τ_P , (or alternatively integration time for a continuous-wave laser). The third term, the probability of scattering, includes the effective absorption cross section, σ_{eff} , (with the assumption that the quantum yield is 100%, meaning that every absorbed photon leads to an emitted photon), He* number density, n_s , and the range bin (i.e., interaction or integration length), Δz . The probability of receiving is the ratio of the receiver telescope area, A_R , to the surface area of a sphere, since He* emits in 4π steradians, whose radius is the range z . Finally, N_B includes any background noise and τ_{int} is the system integration time. In the shot noise limit, the SNR is proportional to $\sqrt{N(z)}$. Of those terms the system designer can control, power and telescope area are the most crucial. While one can increase, for example, Δz , to raise $N(z)$, there is an obvious trade-off in spatial resolution. The power-aperture product ($P_L \times A_R$), on the other hand, can be increased without a cost in resolution.

To measure winds, a multi-frequency approach is needed, requiring that the laser source be tunable. The well-known three-frequency approach [5] is illustrated in Fig. 4. The laser is tuned from the center frequency to frequencies to the blue and red of the center in regular intervals. The desired integration time usually sets the time interval. The “rest” absorption spectrum at 1000 K is shown as the solid blue curve. An arbitrarily Doppler-shifted spectrum is shown as the dashed blue line. Since the absorption cross-sections at wavelengths λ_2 and λ_3 have changed, then the relative received power must also commensurately change. By taking the ratio of their respective returns, information about the windspeed can be deduced. Similarly, an increase in temperature will broaden the spectrum with the major consequence being a reduction in the cross-section at the center frequency. Therefore, by taking the relative ratios of the returns at each of the three wavelengths, windspeed and temperature can be distinguished. Note that since the system looks in the vertical direction, windspeeds are those associated with the vertical component of wind. To measure the radial winds would require transmitting the beam off-zenith and steering the receiving telescope.

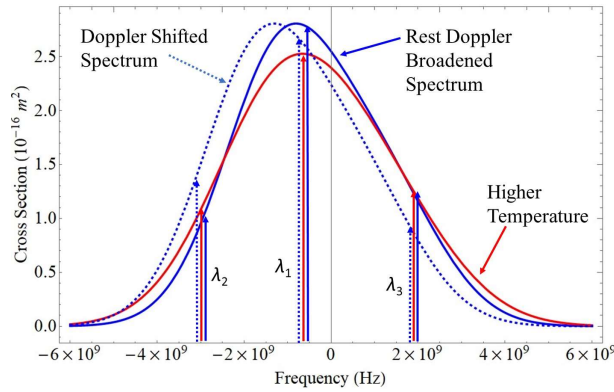


Fig. 4. The three-frequency approach to wind and temperature measurements. The laser is switched between three frequencies. Tracking the relative ratio of returns between the three lines enables the deduction of windspeed and temperature. The vertical arrows are slightly offset for visual clarity.

4. LASER TECHNOLOGY

Rare earth (RE) doped fiber lasers are now a commercially ubiquitous technology. Producing > 10 kW in a single, continuous-wave (CW) beamline, their applications in the industrial manufacturing marketplace continue to grow in number [6-8]. Fiber lasers are attractive mainly because they are widely recognized to be efficient “brightness converters” for multimode, high-wall-plug-efficiency semiconductor pump laser technology [9]. Brightness is the power per unit area per unit solid angle, so it essentially defines a spot size and divergence angle, with low brightness sources having large divergence angle-beam diameter products. The principle behind brightness conversion is that pump light is coupled into the low brightness (large diameter and numerical aperture (NA)) active fiber inner cladding, which is usually coated with a low-index material to guide light. The rare earth doped core then slowly absorbs pump light. An input signal results in stimulated emission (gain), converting the absorbed pump photons to signal photons that are guided in the much higher-brightness core. A simple way to think about this is that the fiber converts a far from diffraction-limited light source (e.g., an array of semiconductor lasers) into a diffraction limited one (fiber laser or amplifier). Although a simplified block diagram is provided in Fig. 5, there are a wide range of fibers and configurations used in building fiber laser systems [10,11]. The fibers themselves may be solid, solid-microstructured, porous-microstructured, and fabricated from a wide range of glass materials [12].

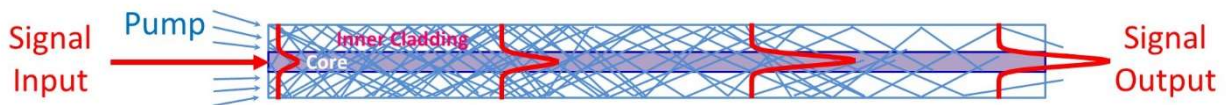


Fig. 5. Schematic of a double clad fiber for high power fiber lasers. Pump light is coupled into the low-brightness inner cladding, slowly absorbed, and then converted to high-brightness signal power in the core.

Owing to their relatively long upper state lifetimes (~ 0.1 to 10 ms, depending on the active dopant, glass host composition, and transition), fiber lasers can be efficiently pulsed, via both Q-switching and mode-locking. They can produce large pulse energies, and peak powers near the damage threshold of glass, with near diffraction-limited beam quality [13-15]. Such systems typically are seeded by a wavelength- and/or temporally controlled source such as an externally modulated semiconductor laser. As such, fiber lasers, both CW and pulsed, can possess extremely narrow linewidths [16].

In pulsed mode, fiber lasers can have transform-limited spectra, whose widths, with long pulses, can be less than a few MHz. This makes them particularly attractive for spectroscopic sensing applications, including LIDAR. Furthermore, the broad emission spectra from rare earth transitions in glass afford continuous wavelength tunability, which is essential for a spectroscopic system. Much of the development of spectroscopic fiber laser-based lidars has focused on sensing and quantifying atmospheric gases, such as water vapor (Nd- and Tm-doped fibers) [17,18], carbon dioxide (Er-doped fibers) [19], and helium (Yb-doped fibers) [4]. These systems can be configured to also provide temperature and wind distributions in different parts of the atmosphere, ranging from the troposphere through the exosphere (1000 km altitude [4], as discussed here). Nonlinear post-processes, such as frequency doubling, Raman shifting, etc. also can increase the wavelength reach of fiber lasers (from just the transitions of the rare earths) to sense pollutants and greenhouse gases, including NO₂, SO₂, and O₃. Such systems can be critical in understanding global energy circulation models, quantifying global warming and climate change, and pollution control. Pulsed lasers enable range-resolved measurements, as opposed to column integration afforded by CW systems [20] in monostatic lidars, giving a full three-dimensional mapping of the quantities being measured. Finally, SWaP (Size, Weight, and Power) considerations make these sources attractive for both airborne and spaceborne platforms.

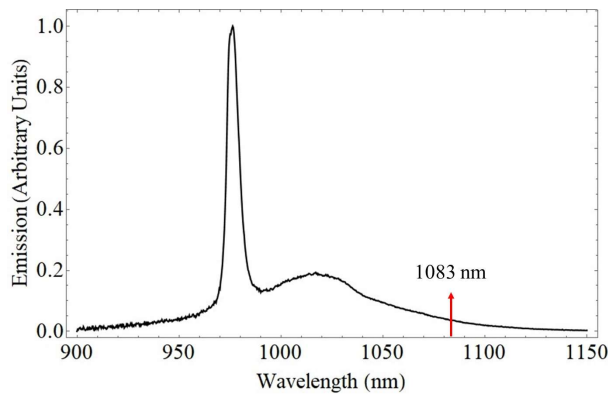


Fig. 6. Spontaneous emission spectrum from an Yb-doped optical fiber identifying 1083 nm. Longer relative operating wavelengths typically require longer optical fibers for efficient operation.

Yb-doped optical fibers currently offer the highest powers and efficiencies of all the rare earth doped fibers. These form the backbone of the commercially available multi-kW systems. Serendipitously, these gain media support efficient amplification of light at 1083 nm which can excite the $2^3S_1 \rightarrow 2^3P_{1,2}$ transition in He*. Fig. 6 provides a spontaneous emission spectrum for a Yb-doped optical fiber. However, narrow linewidth (less than about 50 MHz) fiber lasers are limited in output power due to a process known as stimulated Brillouin scattering (SBS). SBS is an acousto-optic interaction that limits the power per unit bandwidth that can be produced by the fiber laser or amplifier system. The process is not difficult to visualize. It begins with the fiber and its possession of a Langevin bath of thermally generated acoustic noise (random acoustic waves at all frequencies) [21]. These acoustic waves are pressure waves, which, through the photoelastic effect, give rise to refractive index ‘waves’ or perturbations in the fiber. The propagating signal can interact with these acoustic waves, especially those that are phase matched to it in accordance with the Bragg condition. The wavelength of these Bragg-matched waves is given by $\lambda_B = \lambda_o/2n$ where λ_o is the optical wavelength and n is the refractive index (effective mode index in the case of optical fiber). The frequency of the acoustic waves (ν_B) then is determined from $V_A = \nu_B \lambda_o$. Given acoustic velocities (V_A) of around 5000 m/s in silicate glass, relevant acoustic frequencies are around 16 GHz (hypersonic) at 1083 nm.

The forward-propagating optical wave is weakly back-scattered by the (also forward-propagating) Bragg-matched acoustic wave. The backward-propagating scattered optical wave, also having acquired a Doppler Stokes’ shift, proceeds to interfere with the forward-going wave. The resulting interference pattern, through electrostriction, creates a Bragg matched refractive index grating that essentially is an amplified and coherent version of the original Bragg-matched acoustic noise. In other words, amplification of the Bragg matched acoustic wave occurs. This grating increases the strength of back-scatter, and as the optical power is increased, this process becomes

increasingly efficient. At some (somewhat arbitrarily) defined threshold power the effects of SBS become severely detrimental to the laser, including a significant backward-propagating laser signal that can damage components, and output powers that are highly stochastic in time [22]. The SBS threshold, or in other words laser power limit, applies equally to pulsed or continuous-wave (CW) systems. Specifically, if the power limit is 1 kW, that limitation applies to the peak power in pulsed mode (for relatively longer pulses, greater than 10's of nanoseconds) as well as power in a CW system. State-of-the-art, narrow linewidth fiber lasers are currently limited to about 1 kW. There are multiple ways to suppress SBS [23], but this is somewhat beyond the scope of this paper. This limit is in a *single fiber*. Fortunately, these fiber lasers may be coherently combined into phased arrays [24], thereby scaling the output power.

5. TRANSMITTER CONFIGURATION

There is a wide range of laser configurations that can serve the purpose of a high power lidar. However, to keep the discussion brief, a long-pulse fiber laser transmitter is assumed here. Not intending to float concepts that require too much advancement in laser technology, it is further assumed, only somewhat generously, that a 10-element array of 1 kW (SBS-limited) fiber lasers is available that operates at 1083 nm. Neglecting efficiencies in beam combining, this gives 10 kW of optical power in total. These lasers may operate CW for industrial or defense applications, but in pulsed mode SBS still limits the total available peak power to 10 kW. Therefore, with the fixed peak power, to increase the number of transmitted photons the laser pulse width (in length units) is preferably equal to the range bin. Mathematically, this is represented as $\tau_p = 2\Delta z/c$. If the range bin, for example, were arbitrarily selected to be 10 km, one arrives at $\tau_p = 66.7 \mu s$ yielding a pulse energy of 0.67 Joules.

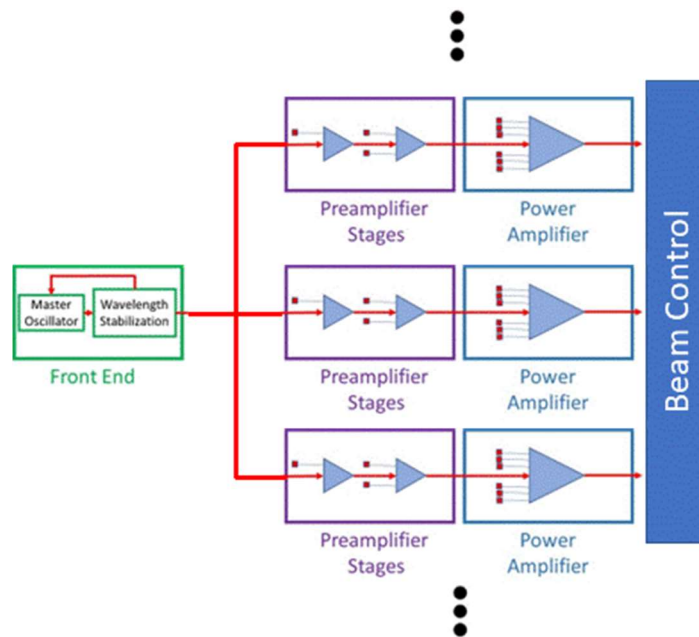


Fig. 7. Simple MOPA laser configured into an N -element array. The Front End, consisting of a laser operating at 1083 nm and with narrow linewidth is stabilized by locking to an external helium gas cell. The power from the Front End may be power-split and serve as master oscillator for all elements in the array. Several preamplifier stages bring the power to a level that makes the Power Amplifier operate very efficiently. The small red squares are the pumps, and they are controlled electrically by switching the supplied current on-and-off.

Such long pulses are very difficult to achieve in any laser. As a result, the “laser” is required to be a gain-switched amplifier, such as via a master oscillator power amplifier (MOPA) arrangement [25]. In such a system (shown simplified in Fig. 7), the pumps in the amplifier stages may be switched on-and-off. If the pump pulse is long enough (usually greater than 10 μs) then the laser can reach steady state and laser output closely mimics the pump timing. To illustrate this, a simple timing diagram is provided in Fig. 8. In this case, the pumps are switched on-and-

off. When operating CW, the laser array can provide 10 kW of power, representing steady state operation. For the most part, switching the pumps on-and-off simply does the same to the laser output. However, depending on the pump wavelength and power, fiber geometry, etc., the amplifier will take some time to reach the steady state, as indicated by the rising edges in the output pulses of Fig. 8. While a full, detailed laser rate equation analysis to demonstrate and illustrate the dynamics is beyond the scope of this paper, rise times on the order of 10 μ s can be expected. If the pumping pulses are much shorter than this value, then the laser (rather, amplifier) will be unable to reach the maximum output power and pulse energy will be degraded.

Other transmitter considerations include the pulse repetition frequency (PRF) which should be set to substantially prevent signal aliasing. Setting the PRF to 100 Hz represents a range of 1500 km, reasonably beyond the end of the He* layer and where the returns approach very small values. Furthermore, since a coherent array may have a near-diffraction limited beam, the desired beam divergence can be achieved by properly setting the beam diameter. This is important from the perspective of receiver field-of-view and its spatial overlap with the laser beam. Finally, since the laser is an amplifier chain, it is assumed that the master oscillator may be power-split and serve as a sufficient seed for all elements in the array

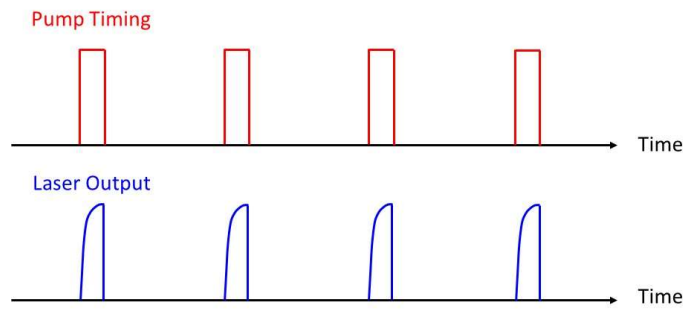


Fig. 8. Pulsed laser timing. The pumps to the amplifier are switched on-and-off (top graph). After a characteristic rise time, the laser output (bottom graph) reaches steady state value of 10 kW. The falling edge of the output pulse will depend somewhat on the master oscillator timing. Not to scale.

6. EXAMPLE RETURNS CALCULATIONS

In this section, lidar simulations with the laser system described above (rise times neglected) are presented. While globally there are several options, the large-aperture telescope at Cerro Pachón, Chile is selected for the present calculations. Regarding the receiver, the responsivity of silicon drops significantly at 1083 nm and cooling the receiver only makes that worse. Alternate materials, such as HgCdTe or InGaAs receivers, though they must be cooled, can have very high quantum efficiency (QE) in the near IR. The overall receiver efficiency, which includes the receiver QE and any losses to the optics, etc., is assumed to be 10%. Furthermore, it is assumed that the system makes use of a notch-pass filter so that any background can be neglected, giving a system operating, ideally, in the shot noise limit. Table 1 summarizes the parameters used in the simulations.

Table 1. Parameters utilized in the simulations.

Parameter	Value
Pulse Energy	0.67 J or 3.33 J
Pulse Width	66.7 μ s or 333 μ s
PRF	100 Hz
Average Power	66.7 W or 333 W
Integration Time	60 s
Range Bin	10 km or 50 km
Receiver Efficiency	0.1
Telescope Area	9.62 m ²

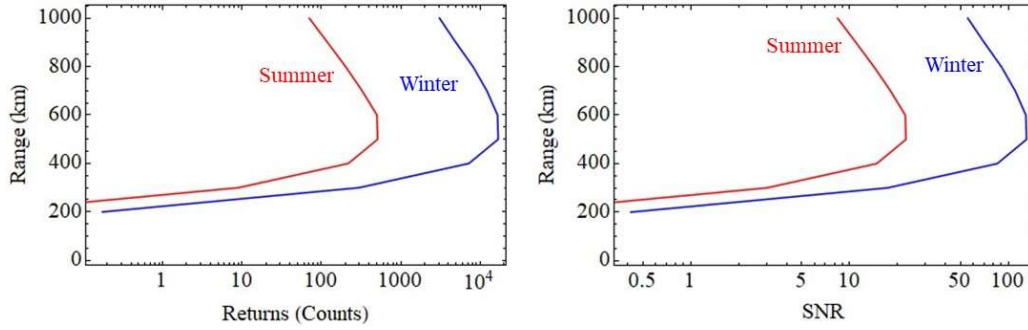


Fig. 9. Lidar returns and SNR calculation for the parameters given in Table 1 with the wavelength set to the maximum He* absorption. Note if two values were provided in the table, these plots correspond to the first of the two. SNR of 10 or above is available nearly across the entire range over the whole year.

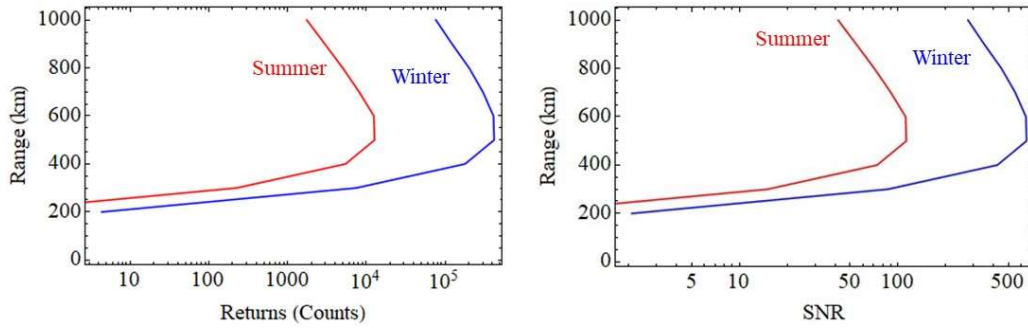


Fig. 10. Lidar returns and SNR calculation for the parameters given in Table 1. Note if two values were provided, these plots correspond to the second of the two. The large available SNR, nearly across the entire range over the whole year, suggests that the integration time can be reduced from 1 minute.

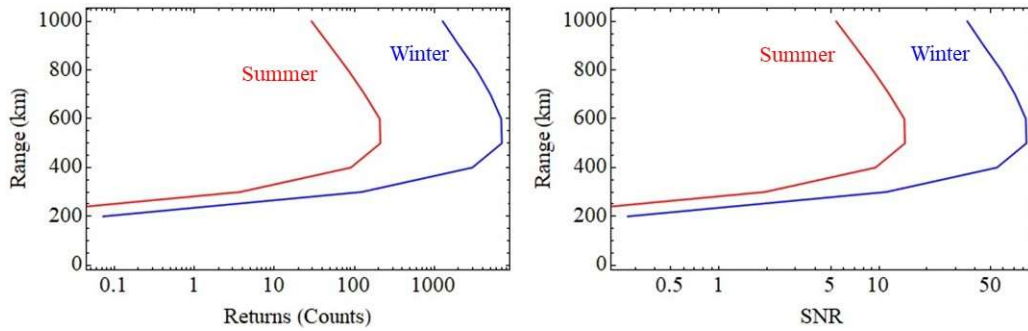


Fig. 10. Lidar returns and SNR calculation from Fig. 10 with the integration time reduced from one minute to one second. Very good SNR, nearly across the entire range, is available in the winter. In summer there is a smaller range of altitudes where the SNR is greater than 10.

The results of the first set of calculations are shown in Fig. 9. Where two values are listed in Table 1, this simulation uses the first of the two. In the shot noise limit, an SNR greater than 10 can be achieved nearly across the whole altitude range over the entire year. As expected, the SNR drops considerably in the summer due to a much lower He* concentration. The second set of calculations, shown in Fig. 10, demonstrates the tremendous enhancement in

SNR if the system spatial resolution were acceptably lower. This implies that the measurement integration time can be reduced from 1 minute. To show this, one final calculation is performed. Specifically, the values from the simulation shown in Fig. 10 are changed only in that the integration time is reduced to one second from one minute. At a PRF of 100 Hz, this means 100 laser shots. These results are provided in Fig. 11. It can be seen that, in winter, very good SNR is available nearly through the whole layer of He*. In the summer, on the other hand, again due to the lower He* concentrations, the SNR is greater than 10 in only a narrow range of altitudes. While a single laser configuration is considered here, other arrangements are discussed at the conference.

7. CONCLUSIONS AND FUTURE WORK

It has been shown that by leveraging modern high-power laser technologies and large aperture telescopes (or even arrays of smaller telescopes), a Doppler wind and temperature resonance fluorescence lidar, enabling rapid and range-resolved measurements of neutral winds and temperatures in the thermosphere and lower exosphere, is within reach. While there are several system level tradeoffs with respect to range resolution, wind and temperature sensitivity, and integration time, much is still unknown about that region of the atmosphere. Without a first set of measurements, it is unclear how to begin defining optimal system parameters (i.e., the system requirements such as “do we integrate for 1 second or 10 minutes?”). Due to the importance of that region of the atmosphere, especially as it relates to space weather, space situational awareness, the movement of energy, etc., let this be a call to the community to support the development of these advanced next-generation systems. As telescopes get larger and laser power increases, these active systems will only improve in performance. This paper was limited to simple calculations of returns and SNR. However, from a system perspective there are still several outstanding design issues that must be addressed. First, the sizeable pulse energies require considering significant low altitude returns from dust, aerosols, or Rayleigh scattering. Second, system alignment is critical given the range, and the identification of true zenith is needed while in operation. Third, with sufficient power, it may be possible to saturate the He* region, limiting the number of return photons. These issues are briefly discussed at the conference.

8. ACKNOWLEDGEMENTS

Authors (PD and GS) gratefully acknowledge the Air Force Office of Scientific Research DURIP grant FA9550-21-1-0298.

9. REFERENCES

- [1] J Bishop and R Link, He(2³S) densities in the upper thermosphere: Updates in modeling capabilities and comparisons with midlatitude observations, *J. Geophys. Res.*, 104(A8):17157–17172, 1999.
- [2] LS Waldrop, RB Kerr, SA González, MP Sulzer, J Noto and F Kamalabadi, Generation of metastable helium and the 1083 nm emission in the upper thermosphere, *J. Geophys. Res.*, 110:A08304, 2005.
- [3] A Gerrard, TJ Kane, DD Meisel, JP Thayer, and RB Kerr, Investigation of a resonance lidar for measurement of thermospheric metastable helium, *J. Atmos. Solar-Terr. Phys.*, 59(16):2023–2035, 1997.
- [4] CG Carlson, PD Dragic, RK Price, JJ Coleman, and GR Swenson, A narrow-linewidth, Yb fiber-amplifier-based upper atmospheric Doppler temperature lidar, *IEEE J. Sel. Top. Quantum Electron.*, 15(2):451-461, 2009.
- [5] CY She and JR Yu, Simultaneous three-frequency Na lidar measurements of radial wind and temperature in the mesopause region, *Geophys. Res. Lett.* 21(17):1771-1774, 1994.
- [6] M Sokolov, A Salminen, M Kuznetsov, and I Tsubulskiy, Laser welding and weld hardness analysis of thick section S355 structural steel, *Mater. Des.* 32:5127-5131, 2011.

- [7] M Zhang, G Chen, Y Zhou, and S Liao, "Optimization of deep penetration laser welding of thick stainless steel with a 10 kW fiber laser," *Mater. Des.* 53:568-576, 2014.
- [8] DAV Kliner et al., (+29 authors), 4-kW fiber laser for metal cutting and welding, *Proc. SPIE* 7914:791418, 2011.
- [9] D Petring, F Schneider, N Wolf, and V Nazery, The relevance of brightness for high power laser cutting and welding, *Presented at ICALEO 2008*, paper 206, 2008.
- [10] M Zervas and C Codemard, High Power Fiber Lasers: A Review, *IEEE J. Sel. Top. Quantum Electron.* 20:0904123, 2014.
- [11] C. Jauregui, J Limpert, and A Tünnermann, High-power fibre lasers, *Nat. Photonics* 7:861-867, 2013.
- [12] PD Dragic, M Cavillon, and J Ballato, Materials for optical fiber lasers: A review, *Appl. Phys. Rev.* 5:041301, 2018.
- [13] F DiTeodoro, JP Koplow, SW Moore, and DAV. Kliner, Diffraction-limited, 300-kW peak-power pulses from a coiled multimode fiber amplifier, *Opt. Lett.* 27:518-520, 2002.
- [14] A Galvanauskas, M-Y Cheng, K-C Hou, and K-H Liao, High Peak Power Pulse Amplification in Large-Core Yb-Doped Fiber Amplifiers, *IEEE J. Sel. Top. Quant. Electron.* 13:559-566, 2007.
- [15] Z Liu, ZM Ziegler, LG Wright, and FW Wise, Megawatt peak power from a Mamyshev oscillator, *Optica* 4:649-6554, 2017.
- [16] D Walton, S Gray, J Wang, M-J Li, X Chen, AB Ruffin, J Demeritt, and L Zenteno, High power narrow linewidth fiber lasers, *Proc. SPIE* 6102:610205, 2006.
- [17] LM Little and GC Papen, Fiber-based lidar for atmospheric water-vapor measurements, *Appl. Opt.* 40:3417-3427. 2001.
- [18] RJ DeYoung, Profiling atmospheric water vapor using a fiber laser lidar system, *Appl. Opt.* 49:562-567, 2010.
- [19] AW Yu et al., (+18 authors), Fiber-Based Laser Transmitter at 1.57 μm for Remote Sensing of Atmospheric Carbon Dioxide from Satellites, *Advanced Solid State Laser Conference*, paper ATh1A, 2015.
- [20] JT Dobler, FW Harrison, EV Browell, B Lin, D McGregor, S Kooi, Y Choi, and S Ismail, Atmospheric CO₂ column measurements with an airborne intensity-modulated continuous wave 1.57 μm fiber laser lidar, *Appl. Opt.* 52:2874-2892, 2013.
- [21] RW Boyd, K Rzaewski, and P Narum, Noise initiation of stimulated Brillouin scattering, *Phys. Rev. A* 42:5514-5521, 1990.
- [22] PD Dragic, Injection-Seeded Q-Switched Fiber Ring Laser, *IEEE Phot. Technol. Lett.* 16:1822-1824, 2004.
- [23] P Dragic and J Ballato, "A brief review of specialty optical fibers for Brillouin-scattering-based distributed sensors, *Appl. Sci.*, 8(10):1996, 2018.
- [24] A Klenke, M Müller, H Stark, F Stutzki, C Hupel, T Schreiber, A Tünnermann, and J Limpert, Coherently combined 16-channel multicore fiber laser system, *Opt. Lett* 43(7):1519-1522, 2018.
- [25] Y Huang, P Yan, Z Wang, J Tian, D Li, Q Xiao, and M Gong, 2.19 kW narrow linewidth FBG-based MOPA configuration fiber laser, *Opt. Express* 27(3):3136-3145, 2019.